

Binary fraction of O and B-type stars from LAMOST data

Feng Luo^{1,2}, Yong-Heng Zhao^{1,2}, Jiao Li^{1,2}, Yan-Jun Guo^{2,4} and Chao Liu^{2,3}

¹ National Astronomical Observatories, Chinese Academy of Sciences, Beijing 100012, China;

² University of Chinese Academy of Sciences, Beijing 100049, China;

³ Key lab of Space Astronomy and Technology, National Astronomical Observatories, Beijing, 100101, China; *liuchao@nao.cas.cn*

⁴ Yunnan observatories, Chinese Academy of Sciences, P.O. Box 110, Kunming, 650011, China;

Received 20xx month day; accepted 20xx month day

Abstract Binary stars plays important role in the evolution of stellar populations . The intrinsic binary fraction (f_{bin}) of O and B-type (OB) stars in LAMOST DR5 was investigated in this work. We employed a cross-correlation approach to estimate relative radial velocities for each of the stellar spectra. The algorithm described by [Sana et al. \(2013\)](#) was implemented and several simulations were made to assess the performance of the approach. Binary fraction of the OB stars are estimated through comparing the uni-distribution between observations and simulations with the Kolmogorov-Smirnov tests. Simulations show that it is reliable for stars most of whom have 6, 7 and 8 repeated observations. The uncertainty of orbital parameters of binarity become larger when observational frequencies decrease. By adopting the fixed power exponents of $\pi = -0.45$ and $\kappa = -1$ for period and mass ratio distributions, respectively, we obtain that $f_{bin} = 0.4^{+0.05}_{-0.06}$ for the samples with more than 3 observations. When we consider the full samples with at least 2 observations, the binary fraction turns out to be $0.37^{+0.03}_{-0.03}$. These two results are consistent with each other in 1σ .

Key words: binaries: spectroscopic — techniques: radial velocities — stars: early-type

1 INTRODUCTION

Binary stars play a crucial role in the evolution of stars and galaxies ([Chini et al. 2012](#), [Almeida et al. 2017](#)). Almost a half of solar-type stars locate in binary systems ([Raghavan et al. 2010](#), [Moe & Di Stefano 2017](#)). A nearby companion would probably affect the evolution of massive stars in binary systems ([Podsiadlowski et al. 1992](#), [Langer et al. 2008](#), [Eldridge et al. 2011](#)), leading to phenomena such as stellar mergers, X-ray binaries and gamma-ray bursts ([Sana et al. 2012](#)). Therefore, it is non-trivial to identify binary system from single stars and to determine the orbital parameters of the binary stars in different Galactic environments

Compared the distance to earth, the separations of most binaries are too close to resolve in photometry. When orbital periods are relative short, 1000 days for example, there are two cases that binaries can be detected through spectroscopic approaches. On one hand, spectra will appeared split or contained "double lines" if the primary and secondary have near degree of luminosities (Pourbaix et al. 2004, Fernandez et al. 2017, Merle et al. 2017). Bimodal peaks would emerge in the cross-correlation function of spectra for these binary systems. On the other hand, the luminosity of secondary is much smaller than primary and it can not contribute enough flux to the spectrum. But, it can lead to orbital motion of primary and bring distinguishable radial velocity (RV) variation (Minor 2013, Troup et al. 2016, Price-Whelan et al. 2017, Badenes et al. 2018). In this paper, we studied the latter case.

A few previous works have studied the intrinsic binary fraction f_{bin} in different environments in the past decades. Raghavan et al. (2010) reported that f_{bin} of solar-type stars is about 0.34. OB stars are considered having a larger binary fraction in some literatures. For B-type stars, Chini et al. (2012) showed that the f_{bin} is 0.46 ± 0.03 . Dunstall et al. (2015) found that there is a relatively high f_{bin} which is 0.58 ± 0.11 . For O-type stars, 0.42 ± 0.04 was came up with Aldoretta et al. (2015), 0.50 ± 0.03 with Sota et al. (2014), 0.51 ± 0.07 with Kobulnicky et al. (2014), 0.68 ± 0.03 with Chini et al. (2012), and 0.69 ± 0.09 with Sana et al. (2012) respectively. The different results of f_{bin} may caused by different methods or data samples adopted in previous researches. These studies seem to reveal that most early type stars are residing in binary systems. The results of binary fraction studied by above-mentioned works are listed in Table.1.

f_{bin}	Number of samples	Spectral type	reference
0.34 ± 0.02	454	FGK	Raghavan et al. (2010)
0.46 ± 0.03	226	B	Chini et al. (2012)
0.58 ± 0.11	408	B	Dunstall et al. (2015)
0.42 ± 0.04	161	O	Aldoretta et al. (2015)
0.50 ± 0.03	194	O	Sota et al. (2014)
0.51 ± 0.07	45	O	Kobulnicky et al. (2014)
0.68 ± 0.03	243	O	Chini et al. (2012)
0.69 ± 0.09	71	O	Sana et al. (2012)

Table 1: Overview of recent studies of binary fraction of different samples.

LAMOST telescope can obtain at most 4000 spectra within one observation and hence can survey the sky in a very high efficiency (Cui et al. 2012, Zhao et al. 2012). The LAMOST targets mainly on stars and its data is widely used in researches of stellar physics and the Milky Way. Its data release 5 (DR5) contains 9,027,634 spectra obtained between October 24, 2011 and June 16, 2017.

The primary goal of this study is to estimate the binary fraction of OB stars observed with LAMOST. At the same time, the distribution law of orbital parameters were explored. Observations of different epochs for a same source may obtain different radial velocities, then binaries can be discriminated from single stars from RV variation. We employ the method proposed by (Sana et al. 2013, hereafter S13), to estimate the f_{bin} for the LAMOST OB stars with multiple observations. LAMOST sample and data selection are

results of observational data are analyzed in Section 4. Discussion and conclusion are given in Section 5 and 6, respectively.

2 DATA

2.1 Samples from LAMOST

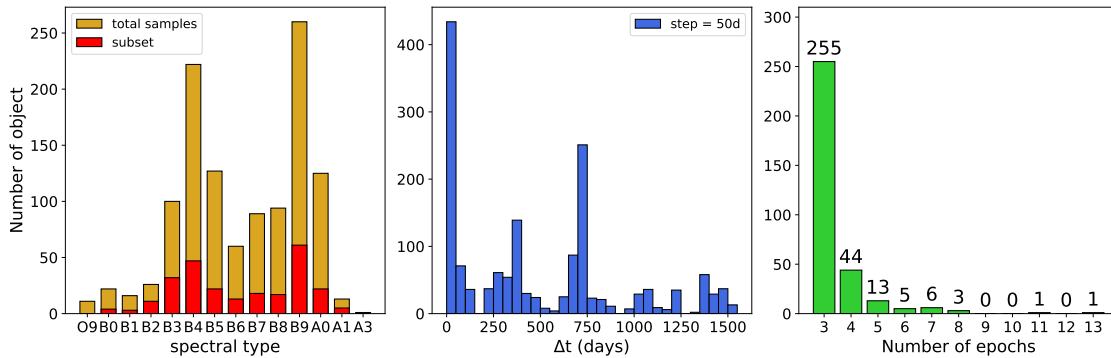


Fig. 1: Left panel: Distributions of the spectral type of the OB stars from Liu et al. (2019) and the subset for this work are presented with yellow and red colours, respectively. Middle panel: It displays the distribution of observational interval of the selected sub-samples. Right panel: It illustrates the distribution of the number of observation for the selected sub-samples.

A catalogue of OB stars from LAMOST released in 2019 (Liu et al. 2019) contains 22,901 spectra of 16,032 stars. 1,715 of them have been targeted with 2 or more epochs by LAMOST. We discard several spectra which $\text{SNR}_g < 10$ or have bad pixels, and leave 1,680 sources for this work. Where SNR_g is the signal-to-noise ratio at g-band, which can be got from the header recorded in the corresponding fits file of each spectrum. Each spectrum was checked by eyes, and pixels with flux equals 0 were regarded as bad pixels.

In general, for a given binary candidate, the more observations we have, the more orbital information we can obtain. Several simulated experiments with mock data were made to assess the capability of repeated observation times to predict orbital parameters. We generated 9 sets of mock samples, each set has the same sample size of 328, the same prior distributions of orbital parameters, but different observation epochs in each set of samples from 2 – 10. The simulated results show that the uncertainty of predictions of orbital parameters becomes smaller when the observational times increase.

According to our experiments, samples who have observed only twice help little to predict the distribution of orbital parameters. Therefore, 328 sources containing 1126 spectra with at least 3 repeated observations were chosen for this study. The distribution of spectral type for the OB stars given by the catalog is shown in the left panel of Fig. 1. Yellow bars indicate the whole samples, while red bars the subset to be used in binarity study. The distribution of time intervals for the repeated observations is shown in the middle panel of Fig.1. The right panel of Fig.1 shows distribution of the number of observations of our

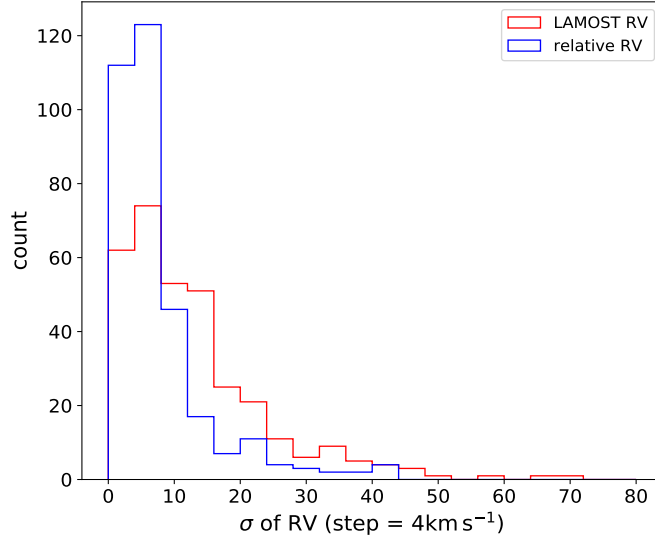


Fig. 2: The uncertainty of RV measurement by cross-correlate method in this paper is about 0.7 km s^{-1} . The blue line displays the distribution of σ_{RV} measured from cross-correlation. The red line shows the distribution of σ_{RV} provided by LAMOST catalog.

2.2 Relative radial velocity

LAMOST pipeline (Luo et al. 2015) provides the doppler shift of each spectrum, which could be used to estimate RV simply by multiplying light speed. However, the doppler shifts in LAMOST RVs are not sufficiently precise for early type stars, since their spectra have fewer lines.

In order to get more precise RVs, we employed a cross-correlation approach to estimate the relative RVs. In general, the usage of template-matching method within a group of spectra corresponding to an observational source that observed at different time can avert the risk of inconsistency of spectral type between the spectrum to be measured and empirical template spectral library, as well as the error brought by this procedure.

The wavelength range used in the cross-correlation analysis depends on the features of OB spectra being considered within the spectral region. Wavelength range of $3900 - 5000 \text{ \AA}$ was chosen because: 1) There are absorption lines such as H_β , H_γ and H_δ in this range which can be used to estimate the relative RV. 2) Many OB stars are brighter at this wavelength range. The wavelength calibration is by use of arc lines, a vacuum wavelength scale is applied for it (Luo et al. 2015).

We chose the spectra with highest SNR_g for each star as the template which relative radial velocity is fixed at zero. Then the rest spectra of the same star were respectively cross-correlated with the template to calculate relative RV. We defined σ_{RV} as the standard deviation of RVs for a given source, which represents the dispersion of the RVs. Results of σ_{RV} calculated by this strategy is showed in Fig. 2, blue line. As a contrast, the red line in Fig. 2 indicated the σ_{RV} provided by LAMOST catalog.

2.3 Error of RV measurement

Binaries can be detected through RV variations. However, the observed RV differences between epochs may

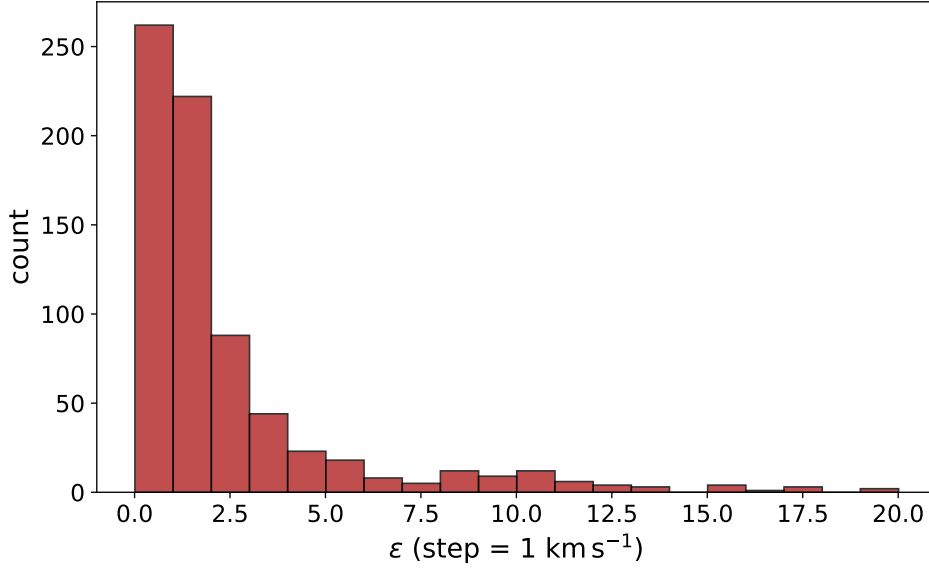


Fig. 3: Distribution of measurement error of RV. The template spectra in each group were not included.

source are composed of both measurement error and doppler shift caused by orbital motion within binary systems. The determination of the measurement error of RV is particularly important because it plays a significant role in the accuracy of our final analysis results.

The measurement error of RV as ε for each spectrum was determined with a Monte-Carlo simulation. For each spectrum we draw 200 spectra with randomly added Gaussian noise. The arbitrarily drawn noise follows sigma as the following.

$$\sigma_{\text{noise}} = \sqrt{\left(\frac{f_{tp}}{snrg_{la}}\right)^2 - \left(\frac{f_{tp}}{snrg_{tp}}\right)^2}, \quad (1)$$

where f_{tp} is the flux of the template, $snrg_{la}$ and $snrg_{tp}$ are SNRg of spectra to be measured and the template, respectively. Then, each spectrum with random noise drawn by Eq. 1 was cross-correlated with its corresponding template to derive the relative RVs. Finally, the uncertainty of RV of each spectrum can be derived from the standard deviation of the RVs of the 200 simulations.

The ε of each template was defined as $10^{-4} \text{ km s}^{-1}$ for the following two reasons. Firstly, to avoid the exception with a divisor of zero, and make sure that the calculations go on wheels. Secondly, it should be defined as a sufficiently small value. The ε of each spectrum was derived from the template-matching method with its corresponding template, but it will be very small for the template spectrum itself. We tested the algorithm by adopting ε as 10^{-3} and $10^{-2} \text{ km s}^{-1}$, there is no change in the final results. The distribution of ε of all sources but the templates is shown in Fig. 3.

3 METHOD

3.1 Introduction to S13 method

There are seven parameters that describe binary orbits as shown in Table.2 The RV equation (Eq.2) can be drawn through the geometric calculation of the motion of elliptic orbit.

$$RV = \frac{2\pi a \sin i}{\gamma} [\cos(\theta + \omega) + e \cos \omega] + \gamma \quad (2)$$

Name	Comment
P	orbital period
q	mass ratio
e	eccentricity
m_1	mass of the primary
i	angle of inclination
ω	longitude of the periastron
T_0	the time of periastron passage

Table 2: Kinematics orbital parameters of binary

where γ is the systemic velocity, or the radial velocity of the center of mass of the binary system. It relates to the motion of the whole system. The γ always equals 0 in our method since the radial velocities measured by template-matching approach within a source are relative radial velocities, which were not include the systemic velocity. a is the long axis of the elliptic orbit of the primary, which is associated with mass ratio q . θ is the position angle between the radius vector and a reference direction, which as a function of the time of an observational epoch. P , e , i , ω and T_0 are defined in Table 2. We thus can get a simulated RV by given a set of the 7 orbital parameters and an observational time.

We implemented the algorithm described by S13. The criteria is based on the detectable obvious change in RVs. A source is deemed a spectroscopic binary star when there is at least one pair of RV satisfies

$$\frac{|v_i - v_j|}{\sqrt{\varepsilon_i^2 + \varepsilon_j^2}} > 4.0 \quad \text{and} \quad |v_i - v_j| > C, \quad (3)$$

where v_i and ε_i are the RV and its error of epoch i for a given object. The value of C was conservatively adopted with 20 km s^{-1} because not only photospheric variations in supergiants can mimic variations with amplitudes of up to 20 km s^{-1} (Ritchie et al. 2009) but also wind effects of some stars (Li et al. 2016, Abdul-Masih et al. 2020). Even though, it is somewhat subjective to give an exact value to C as a cutoff for binary detection. But, the intrinsic binary fraction f_{bin} of real observations will be corrected through the simulation procedure described as below. Therefore, a reasonable selection of C will not significantly affect the final result. For a source with more than 3 observations, several pairs of RVs may satisfy Eq. 3, each pairs corresponds to its own observational time scale ΔHJD . The maximum RV variation ΔRV and the minimum time scale ΔHJD were recorded respectively in two sequences, which will be used to compare with the simulations utilizing Kolmogorov-Smirnov (KS) tests.

Accounting for observational biases due to sampling and measurement uncertainties we need to search for sets of distributions that reproduce the properties of the observations in three aspects: 1) The observed binary fraction; 2) the peak-to-peak amplitude ΔRV of the RV variations; 3) the minimum time scale ΔHJD for significant RV variation to be observed. Simulated and observed distributions are compared by mean of KS tests. The binary fraction detected in the simulations will be compared to the observed fraction using a Binomial distribution Sana et al. (2012). A global merit function (Ξ') is constructed as:

$$\Xi' = P_{KS}(\Delta RV) \times P_{KS}(\Delta HJD) \times B(N_{bin}, N, f_{bin}^{simul}), \quad (4)$$

where f_{bin}^{simul} and N_{bin} are the binary fraction and the number of samples detected in simulated samples.

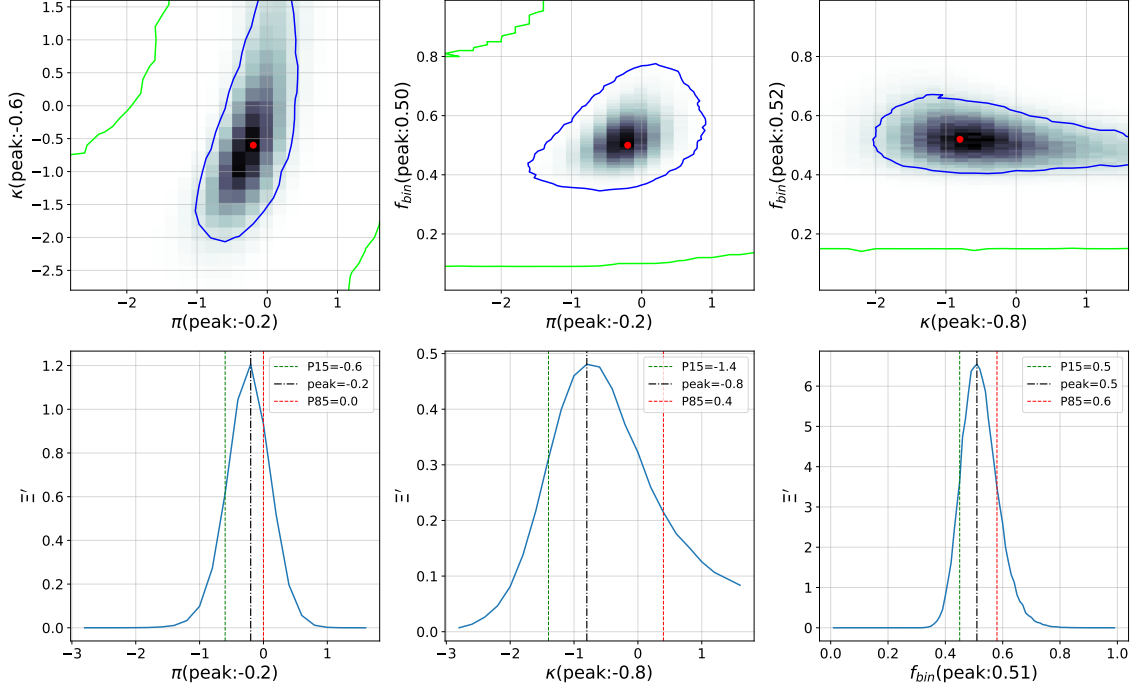


Fig. 4: The figure shows the results using S13 data. Panels in the top row display the projection of Ξ' onto π vs. κ , π vs. f_{bin} and κ vs. f_{bin} respectively. The green and blue contour lines indicate the 15 and 85 percentile of Ξ' . Panels in the bottom row show the projection of Ξ' onto π , κ and f_{bin} respectively. The green and red dotted lines indicate the position of 15 and 85 percentile of Ξ' .

of orbital parameters, e.g., $f(\log_{10} P/d) \sim (\log_{10} P)^\pi$, $f(q) \sim q^\kappa$ and $f(e) \sim e^\eta$ (η is fixed at -0.5). We thus can explore the distribution of Ξ' in the three-dimensional parameter space (π, κ, f_{bin}) by using Monte-Carlo approach.

3.2 Validation

3.2.1 Verification of the algorithm with S13 data

We used the real observational data from S13 to test our code. Following S13, we adopted the detected range of $\log_{10} P$, q and e are $\log_{10} P \in [0.15, 3.5]$, $q \in [0.1, 1.0]$ and $e \in [10^{-5}, 0.9]$, respectively. The results of our program are shown in Fig. 4. Panels in the top row are the projections of Ξ' from the multi-dimensional space onto π vs. κ , π vs. f_{bin} , and κ vs. f_{bin} . Red points indicate the peak positions. In Fig. 4, the bottom panels are one-dimensional Ξ' projections to π , κ , and f_{bin} , respectively.

It is worthy to note that assuming the binary mass ratio follow a power-law distribution may not be very precise (Liu 2019). However, it could tell us approximately about the relative amount of binaries with low and high mass ratio to some extent.

The best-fit parameters displayed in the figure well agree with results by S13. That means we success-

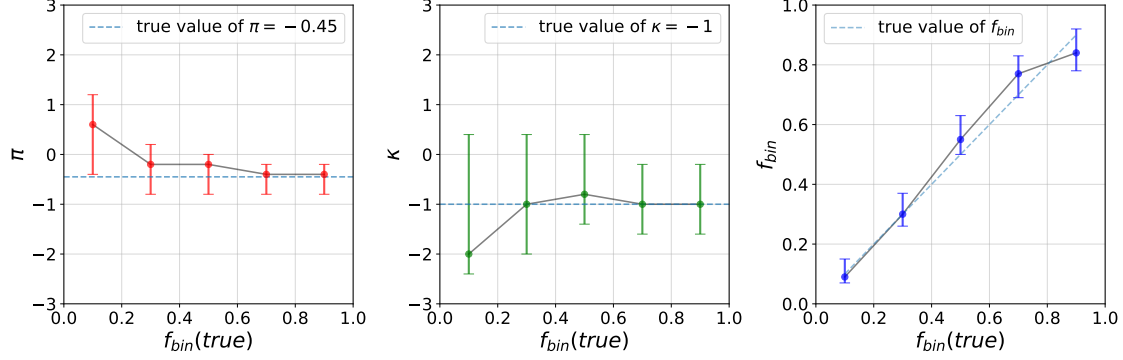


Fig. 5: Results of simulation experiments with mock samples generated based on S13 data. The three panels display the recoveries of π , κ and f_{bin} respectively with different true values of f_{bin} , short transverse lines at the bottom and top of each vertical line indicated the position of 15 and 85 percentile, points between them are peak positions.

3.2.2 Effect of the true f_{bin}

More simulations were carried out to investigate how binary fraction affects the results. We generated 332 mock samples of binaries with $\pi, \kappa, \eta = (-0.45, -1, -0.5)$ (S13) and 332 samples of single stars with measurement error of each spectrum. The number of observations, observational time interval and RV measurement error of simulated binary samples are came from S13 data. The primary mass, m_1 , was randomly drawn from an initial mass function (IMF) described by [Salpeter \(1955\)](#) with mass range from 15 to $80 M_{\odot}$. The rest parameters i, ω, T_0 are randomly drawn from the assumed distributions:

$$\cos i \sim Uniform(0, 1), \quad \omega \sim Uniform(0, 2\pi), \quad T_0 \sim Uniform(0, P). \quad (5)$$

In order to investigate whether the adopted method can accurately estimate f_{bin} , which is the most important parameter, we run the Monte-Carlo procedure with a parameter grid where $\pi \in [-3, 2]$, $\kappa \in [-3, 2]$. And all the following calculations we adopted the fixed $\eta = -0.5$. The simulated samples are given with different initial f_{bin} ranging from 0.1 to 0.9 with a step of 0.2. The results of f_{bin} estimation and predictions of π, κ are shown in Fig. 5. The error bars in each panel indicate the 15 and 85 percentiles, points between top and bottom of error bars are the peak position.

Fig.5 shows that when f_{bin} is low, the predictions of π and κ are inaccurate. The errors of π and κ decrease and the predicted values of π and κ tend to be pinned down at around the ground true values with the increase of f_{bin} . This is in all probability because the estimations of orbital distributions rely on the enough fraction of binary systems.

Our exercise shows that when $f_{bin} > 0.3$ the estimation of π and κ is reliable. From the right panel we can see the the f_{bin} prediction is more accurate than π and κ . This demonstrates that the method is credible at least in the f_{bin} estimation for the mock samples.

3.2.3 Validation with mock data mimic LAMOST samples

We then did the third simulations to investigate whether the LAMOST samples fit the method. Mock sam-

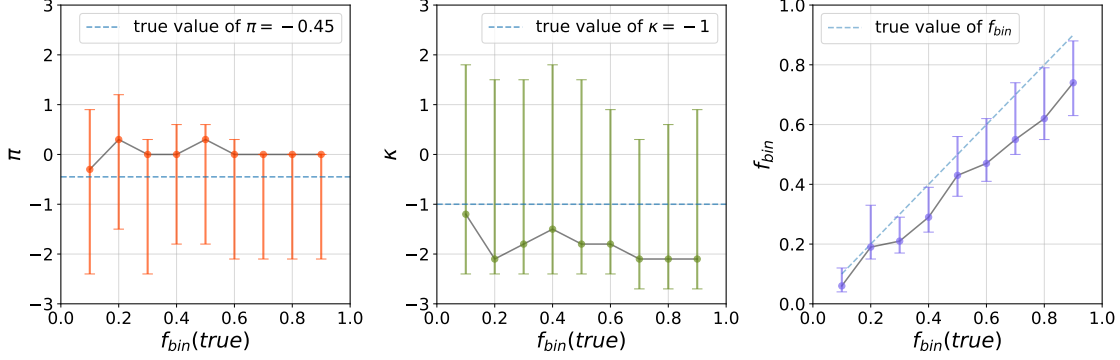


Fig. 6: Results of simulations with mock samples generated based on LAMOST OB samples. The three panels display the recoveries of π , κ and f_{bin} respectively with different true values of f_{bin} , short transverse lines at the bottom and top of each vertical line indicated the position of 15 and 85 percentile, points between them are peak positions.

same way mentioned above but the range of m_1 was from 5 to 20 M_{\odot} . The differences are the value range of $\log_{10} P$ is [0.15, 3.0], and the detection range of π, κ are $\pi \in [-3, 3], \kappa \in [-3, 3]$. The corresponding results are shown in Fig. 6.

The left panel displays the estimation of π , from which we found that there are evident asymmetry and slight overestimates in almost all samples with different f_{bin} . When $f_{bin} = 0.7, 0.8, 0.9$, the corresponding peak values of π overlapped with their correspond 85 percentiles meaning that the probability distribution of π is highly skewed toward large values. The estimation of κ , delineated in the middle panel, shows that there also are obvious asymmetry and underestimations in all cases. Compared with S13 results we find the peak value of κ is skewed toward smaller values. But the skewness may be also caused by the limit of detection range we defined.

From the right panel we can see that f_{bin} estimates are roughly around the ground truth in all cases. However, the derived f_{bin} are slightly underestimated by around 0.1 when the real f_{bin} is smaller than 0.6. When the true value is larger than 0.6, the estimates are underestimated by about 0.15. The different behavior of f_{bin} between Fig.5 and Fig.6 is likely due to the difference of the two dataset especially their differences in observation epochs.

4 RESULT

4.1 Estimation of f_{bin} with open π and κ

By mean of Eq.3, 72 samples were satisfied and are regarded as binary in the 328 OB samples selected in Sect. 2.1. So the observed binary fraction is $72/328 = 0.22$. The calculated results are shown in Fig.7, which layout is similar with Fig.4.

As shown in the top-left panel, the Ξ' range larger than 85 percentile is larger compared to S13 result. The distribution of Ξ' in π vs. κ indicates that the two parameters are correlated to some extent. It seems that Ξ' shows two peaks with irregular shape in top-middle panel.

The f_{bin} and κ are anti-correlated especially when $\kappa < 0$ as shown in top-right panel. A lower κ

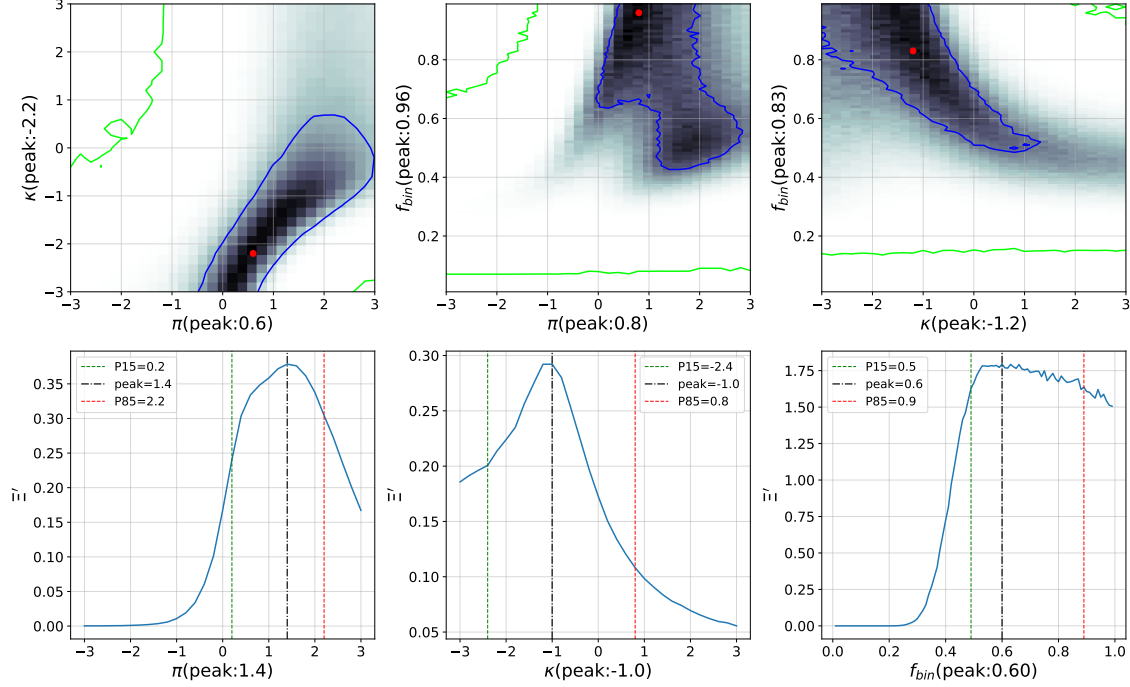


Fig. 7: Results of the LAMOST 328 OB stars with at least 3 observations. Panels in the top row display the projection of Ξ' onto π vs. κ , π vs. f_{bin} and κ vs. f_{bin} respectively. The green and blue contour lines indicate the 15 and 85 percentile of Ξ' . Panels in the bottom row show the projection of Ξ' onto π , κ and f_{bin} respectively. The green and red dotted lines indicate the position of 15 and 85 percentile of Ξ' .

chooses smaller κ more binaries having much lower mass companion. In this case, single stars are easy to contaminate to binary samples. As a consequence, f_{bin} is likely larger. This can well explain the anti-correlation shown in κ vs. f_{bin} plane. The bottom panels display the marginal Ξ' of π , κ and f_{bin} . All the 3 distributions are much broader compared with S13 (also Fig.4). The peak positions of π and κ are 1.4 and -1 (bottom-left and bottom-middle panels in Fig.7). A larger peak value of π means there are relative more binaries with long orbital periods than S13 samples. This may be also caused by fewer observations so that gives a partial result with little statistical significance. The estimation of κ is essentially consistent with S13 with a larger uncertainty.

It seems that the current samples, with less numbers of observations, are hard to simultaneously constrain π , κ and f_{bin} . We then turn to only constrain f_{bin} with the Monte-Carlo procedure by fixing π and κ at -0.45 and -1 , respectively, as concluded by S13.

4.2 Estimation of f_{bin} with fixed π and κ

If π and κ are fixed, a few experiments we made show that the fluctuation of statistics is remarkable when the number of random samplings in Monte-Carlo procedure is 100. In order to weaken the statistical fluctuation, the steps of Monte-Carlo procedure was increased to 2×10^5 . According to Eq. 2, a multi-degree-of-freedom formula implies that more repeated observations were need to predict the distributions of orbital periods and mass ratio. But, the f_{bin} could be estimated when the parameters, π and κ , are fixed. The samples excluded

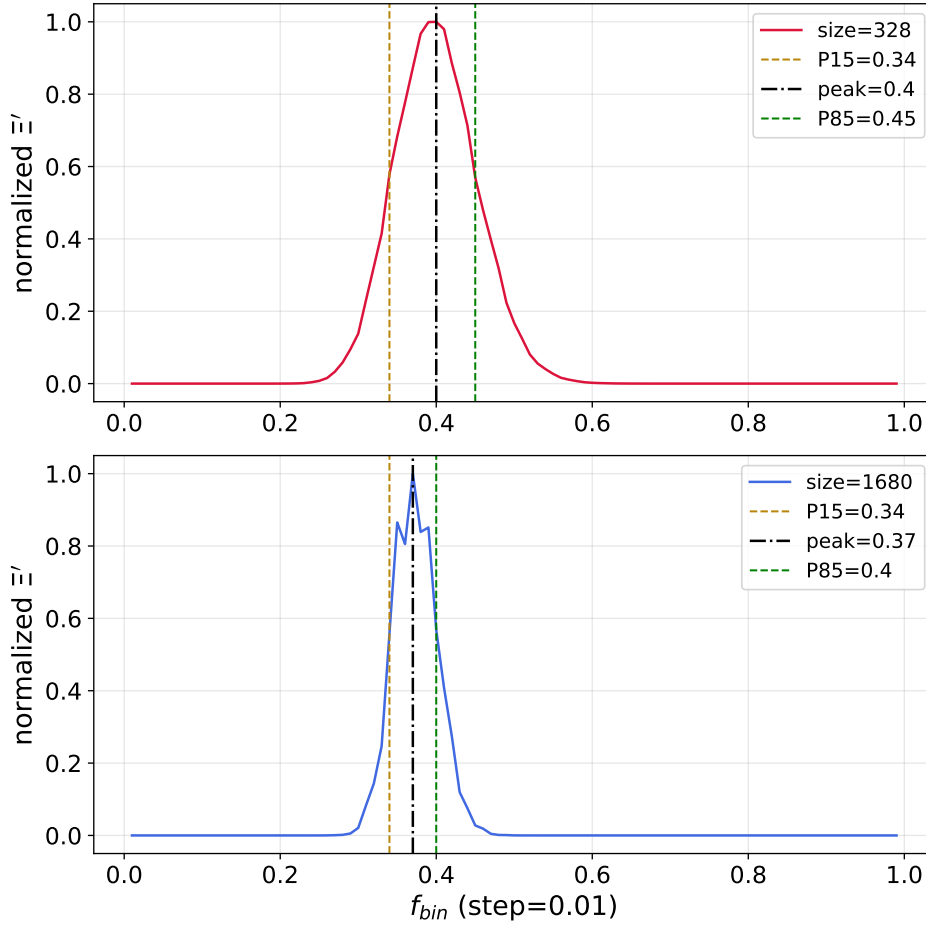


Fig. 8: Estimation of f_{bin} under the condition $(\pi, \kappa) = (-0.45, -1)$. The top panel: It displays the result of subset containing 328 samples. The 15 and 85 percentiles are 0.34 and 0.45 respectively, and the peak position at 0.4. The bottom panel: It shows the result of whole samples containing 1680 stars. The 15 and 85 percentiles are 0.34 and 0.4 respectively, and the peak position at 0.37.

the same time. The observed binary fraction directly derived by Eq. 3 of total samples is 0.15. Calculated results of subset and total samples were shown in Fig. 8. Where the ordinate indicated the normalized Ξ' , and f_{bin} is $0.4^{+0.05}_{-0.06}$ for the subset, and $0.37^{+0.03}_{-0.03}$ for the total samples. The error bar become narrower when number of samples goes up, and the closer peaks shown that the two results are consistent with each other.

Note that, with LAMOST data the adopted S13 method tends to underestimate f_{bin} by about 0.15 (see Fig. 6). Therefore, the real f_{bin} of the OB samples may reach ~ 0.65 . However, since the simulations to produce Fig. 6 are under different conditions, precise systematic correction for f_{bin} is difficult.

5 DISCUSSION

5.1 Number of observation

In the top panels of Fig. 7, it is seen that constraints on π, κ and f_{bin} are not very precise compared with results of S13 shown in Fig. 4. That's because there are 7 parameters, $(P, q, e, m_1, i, \omega, T_0)$, and the time of

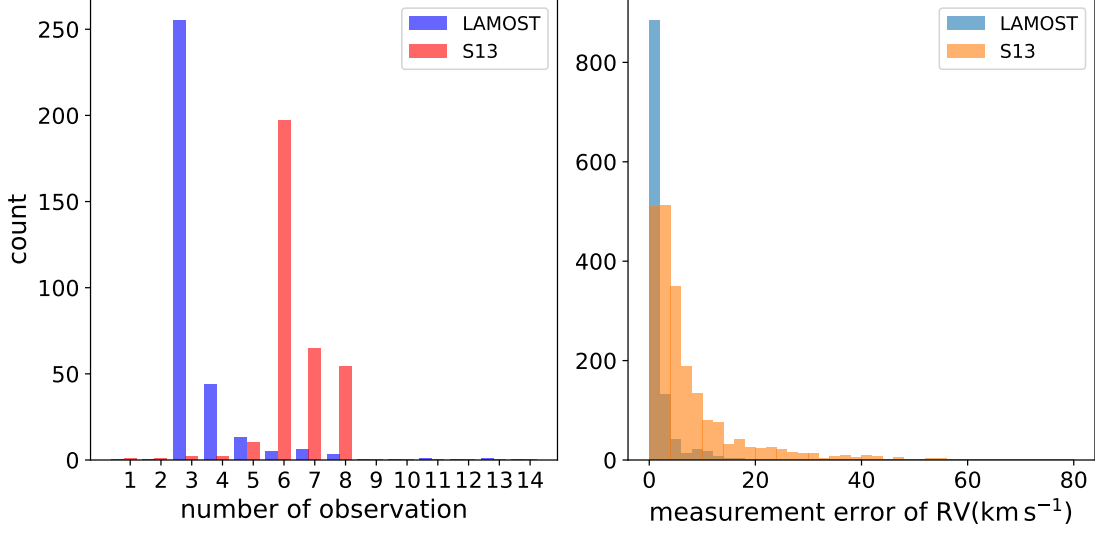


Fig. 9: Left panel: It displays the comparison of number of observation between data from S13 and LAMOST, blue bars indicated LAMOST data, and red bars represented S13 data. Right panel: It depicts the comparison of measurement error of RV between data from S13 and LAMOST, cyan bars indicated LAMOST data, and orange bars represented S13 data.

given source are indispensable to provide sufficient information helping to the parameters determination. However, there are 255 sources in our 328 samples with exactly 3 observations. Fewer information they carried leads to larger uncertainty of the orbital parameter estimates. Number of observations of S13 and our samples are displayed in the left panel in Fig. 9. Most of S13 samples have 6, 7 and 8 repeated observations, but 3, 4 and 5 in our samples. That's the main reason our results is limited by larger uncertainty.

5.2 Measurement error of relative RV

While selecting sources from LAMOST, we filtered samples whose RV measurement error larger than 20 km s⁻¹. The abandoned samples generally have spectra with low SNRg or defective pixels. The samples with larger RV measurements error were contained in S13 data and thus their RV variation may be not very accurate, see right panel of Fig. 9.

5.3 Cutoff of orbital period

The maximum of detection range of $\log_{10} P$, or P , obviously affect the final estimation of f_{bin} . A smaller maximum of P means the model can not detect binaries with orbital periods longer than the maximum. Then, these binaries will be regarded as single stars, and the f_{bin} goes smaller at the same time.

The cutoff of detection range of $\log_{10} P$ of our samples is 3.0, which is smaller than 3.5 adopted by S13. So the final calculated f_{bin} results is smaller than S13 naturally. But, the cutoff of P is not the larger the better. Due to the influences from measurement error of RV, single stars have more risk to fall into binaries

6 CONCLUSION

We applied the method introduced by S13 to estimate the properties of binary stars based on the LAMOST OB samples. We find f_{bin} is $0.4_{-0.06}^{+0.05}$ for the samples with at least 3 observations and $0.37_{-0.03}^{+0.03}$ for the total samples. Many simulations were made to investigate the capability of the S13 method. We find that because the epochs of the LAMOST observations are smaller than S13 samples, π and κ can not be well constrained. In future, we will revisit this problem with LAMOST time-domain data so that π and κ can also be estimated.

Acknowledgements This work is supported by the National Key R&D Program of China No. 2019 YFA0405501. This work is also supported by the National Natural Science Foundation of China with grant Nos. 11835057, 12090040, 12090043. Guoshoujing Telescope (the Large Sky Area Multi-Object Fiber Spectroscopic Telescope LAMOST) is a National Major Scientific Project built by the Chinese Academy of Sciences. Funding for the project has been provided by the National Development and Reform Commission. LAMOST is operated and managed by the National Astronomical Observatories, Chinese Academy of Sciences. This research uses data obtained through LAMOST, which is operated and managed by the National Astronomical Observatories, Chinese Academy of Sciences, and the Special Fund for Astronomy from the Ministry of Finance. *Facilities:* LAMOST *Software:* astropy(Astropy Collaboration et al. 2018),scipy(Virtanen et al. 2020),TOPCAT(Taylor 2005)

References

- Abdul-Masih, M., Banyard, G., Bodensteiner, J., et al. 2020, *Nature*, 580, E11 6
- Aldoretta, E. J., Caballero-Nieves, S. M., Gies, D. R., et al. 2015, *AJ*, 149, 26 2
- Almeida, L. A., Sana, H., Taylor, W., et al. 2017, *A&A*, 598, A84 1
- Astropy Collaboration, Price-Whelan, A. M., Sipőcz, B. M., et al. 2018, *AJ*, 156, 123 13
- Badenes, C., Mazzola, C., Thompson, T. A., et al. 2018, *ApJ*, 854, 147 2
- Chini, R., Hoffmeister, V. H., Nasserri, A., Stahl, O., & Zinnecker, H. 2012, *MNRAS*, 424, 1925 1, 2
- Cui, X.-Q., Zhao, Y.-H., Chu, Y.-Q., et al. 2012, *Research in Astronomy and Astrophysics*, 12, 1197 2
- Dunstall, P. R., Dufton, P. L., Sana, H., et al. 2015, *A&A*, 580, A93 2
- Eldridge, J. J., Langer, N., & Tout, C. A. 2011, *MNRAS*, 414, 3501 1
- Fernandez, M. A., Covey, K. R., De Lee, N., et al. 2017, *PASP*, 129, 084201 2
- Gao, S., Zhao, H., Yang, H., & Gao, R. 2017, *MNRAS*, 469, L68 1
- Kobulnicky, H. A., Kiminki, D. C., Lundquist, M. J., et al. 2014, *ApJS*, 213, 34 2
- Langer, N., Cantiello, M., Yoon, S.-C., et al. 2008, in *Massive Stars as Cosmic Engines*, ed. F. Bresolin, P. A. Crowther, & J. Puls, Vol. 250, 167 1
- Li, C., de Grijs, R., Deng, L., et al. 2016, *Nature*, 529, 502 6
- Liu, C. 2019, *MNRAS*, 490, 550 7
- Liu, Z., Cui, W., Liu, C., et al. 2019, *ApJS*, 241, 32 3
- Luo, A. L., Zhao, Y.-H., Zhao, G., et al. 2015, *Research in Astronomy and Astrophysics*, 15, 1095 4
- Merle, T., Van Eck, S., Jorissen, A., et al. 2017, *A&A*, 608, A95 2

- Moe, M., & Di Stefano, R. 2017, *ApJS*, 230, 15 [1](#)
- Podsiadlowski, P., Joss, P. C., & Hsu, J. J. L. 1992, *ApJ*, 391, 246 [1](#)
- Pourbaix, D., Tokovinin, A. A., Batten, A. H., et al. 2004, *A&A*, 424, 727 [2](#)
- Price-Whelan, A. M., Hogg, D. W., Foreman-Mackey, D., & Rix, H.-W. 2017, *ApJ*, 837, 20 [2](#)
- Raghavan, D., McAlister, H. A., Henry, T. J., et al. 2010, *ApJS*, 190, 1 [1](#), [2](#)
- Ritchie, B. W., Clark, J. S., Negueruela, I., & Crowther, P. A. 2009, *A&A*, 507, 1585 [6](#)
- Salpeter, E. E. 1955, *ApJ*, 121, 161 [8](#)
- Sana, H., de Mink, S. E., de Koter, A., et al. 2012, *Science*, 337, 444 [1](#), [2](#), [6](#)
- Sana, H., de Koter, A., de Mink, S. E., et al. 2013, *A&A*, 550, A107 [1](#), [2](#)
- Sota, A., Maíz Apellániz, J., Morrell, N. I., et al. 2014, *ApJS*, 211, 10 [2](#)
- Taylor, M. B. 2005, in *Astronomical Society of the Pacific Conference Series*, Vol. 347, *Astronomical Data Analysis Software and Systems XIV*, ed. P. Shopbell, M. Britton, & R. Ebert, 29 [13](#)
- Troup, N. W., Nidever, D. L., De Lee, N., et al. 2016, *AJ*, 151, 85 [2](#)
- Virtanen, P., Gommers, R., Oliphant, T. E., et al. 2020, *Nature Methods*, 17, 261 [13](#)
- Zhao, G., Zhao, Y.-H., Chu, Y.-Q., Jing, Y.-P., & Deng, L.-C. 2012, *Research in Astronomy and Astrophysics*, 12, 723 [2](#)